Research Article Vol. 34, No. 4 / 23 Feb 2026 / Optics Express 5788
Optics EXPRESS

Fast and sensitive wavelength modulation gas spectroscopy in micro-drilled hollow-core fiber

ELEANOR A. WARRINGTON,[1] ROBERT PEVERALL,[2] PATRICK S. SALTER,[1] GUS HANCOCK,[2] MARTIN J. BOOTH,[1] GRANT A. D. RITCHIE,[2] AND JULIAN A. J. FELLS[1,*]

[1]*Department of Engineering Science, University of Oxford, Parks Lane, Oxford OX1 3PJ, United Kingdom*
[2]*Department of Chemistry, Physical & Theoretical Chemistry Laboratory, University of Oxford, South Parks Road, Oxford OX1 3QZ, United Kingdom*
[*]*julian.fells@eng.ox.ac.uk*

Abstract: Micro-drilled anti-resonant fiber is demonstrated as a practicable tool for laser-based spectroscopic acetylene sensing, overcoming the slow fiber-filling time usually associated with hollow-core fiber-based methods. Microchannels were drilled through the side of the fiber, periodically along its length, using image processing to accurately target the gap between the capillaries for minimal loss. A 0.3% acetylene / 0.3% methane gas mixture balanced in air was tested in the near-infrared on two micro-machined fiber samples. Wavelength modulation spectroscopy was used to enhance the sensitivity of the detection. A 1 m anti-resonant fiber with microchannels every 5 cm was found to have a minimum detection limit of 380 parts per billion at atmospheric pressure and 100 s acquisition time with a 22 s fiber filling time without the use of a pressure differential. The filling time was 4.2 s for a 30 cm fiber with a closer microchannel separation of 2 cm.

1. Introduction

Many applications, including atmospheric mapping [1] and combustion diagnostics [2], can benefit from using hollow-core fiber as a gas sensing medium [3]. It has the flexibility to enable spatially selective measurements over a long path length while not being restricted to strict line-of-sight and alignment criteria. The sensitivity can be increased by using longer path lengths; however, this can result in a slow response time if relying on diffusion alone to transfer the analyte of interest into the fiber, from the fiber ends. Fiber gas absorption spectroscopy was initially investigated using hollow-core photonic crystal fiber (PCF) [4–8] and the response time improved by inserting holes in the side of the fiber to reduce the diffusion length and hence decrease the diffusion time [6–8]. However, because of the internal structure of the PCF, optical loss was introduced, which limited the achievable sensitivity. More recently, anti-resonant fiber (ARF) has been used [9–18], which consists of a hollow-core surrounded by several non-touching capillaries for light confinement [19–22]. This fiber structure is therefore more suitable for gas detection, where the gas-filled hollow-core can be used as the sensing channel, without altering the light guiding properties of the fiber [23,24]. Pressure filling has previously been used to reduce the diffusion time for both PCF [4,5] and ARF [9–16,18], but it is not always a practical approach, particularly for remote sensing. A summary of these previous demonstrations of fiber gas absorption spectroscopy, found in the literature, is given in Table 1.

Recently, Kozioł *et al.* [25] machined holes in the side of ARF, without damaging the light guiding structure and used it to measure direct absorption spectra [17]. However, the fabrication process meant that there was a 15 cm separation between sections of fiber containing holes, so the diffusion time was as high as 330 s, and the sensitivity was limited by the use of direct absorption.

#583087 https://doi.org/10.1364/OE.583087
Journal © 2026 Received 3 Nov 2025; revised 13 Jan 2026; accepted 14 Jan 2026; published 9 Feb 2026

Optics EXPRESS

Table 1. Summary of a selection of previous relevant work in fiber spectroscopy for gas detection.

	Length of Fiber (m)	Microchannel Seperation (cm)	Pressure Differential?	Gas Detected	Wavelength (μm)	Detection Limit	Time Response (s)
PCF	1.3 [4]	-	✓	CH_4	3.4	1 ppm	<10
	13 [5]	-	✓	C_2H_2	1.53	1 ppmv	-
	0.07 [6]	1	-	CH_4	1.665	647 ppmv	3
	0.48 [7]	12	-	CH_4	1.666	~ 158 ppmv	248
	0.9 [8]	30	-	C_2H_2	1.550	500 ppmv	1200
ARF	1 [9]	-	✓	CH_4	3.334	24 ppbv	19
				CO_2	1.574	114 ppmv	
	1.15 [10]	-	✓	NO	5.26	10 ppbv	~ 9
	0.85 [11]	-	✓	CO	2.3	~ 0.4 ppmv	5
	1.35 [12]	-	✓	CO_2	2	~ 5 ppmv	5
	3.2 [13]	-	✓	NO	4.53	1 ppbv	<30
	0.5 [14]	-	✓	CH_4	3.3	2.24 ppmv	5.4
	7.5 [15]	-	✓	CH_4	3.27	1.54 ppbv	<120
	5 [16]	-	✓	CH_4 dissolved in liquid	1.65	45 ppbv	486
	1.25 [17]	15	-	N_2O	4.57	-	330

As an alternative, photothermal spectroscopy has also been used on ARF with microchannels [26]. However, photothermal spectroscopy is complex to implement, gives an indirect measurement of absorption, and suffers from slow response times. A method of fabricating microchannels through the side of ARF with arbitrarily close separation over arbitrarily long fiber lengths has recently been shown [27]. In this work, sensitive gas spectroscopy is demonstrated on ARF with closely spaced microchannels along its length, fabricated using this technique, and wavelength modulation spectroscopy (WMS) is used to enhance the sensitivity. In this technique, the central frequency is slowly tuned through an absorption feature using a current ramp.

2. Microchannels and diffusion

A thorough description of the microchannel fabrication procedure used is described in [27], including details on microchannel placement and transmission loss. A 790 nm femtosecond laser (Spectra Physics Solstice) with a pulse duration of 140 fs, a 1 kHz repetition rate and a pulse energy of 5.5 μJ was used to fabricate the microchannels through the side of the ARF into the core by laser ablation [27,28]. The fiber was held in a mount which allowed rotation about its transmission axis. The laser beam was focused on the fiber using a 20× 0.5 NA objective. The fiber was imaged onto a CCD camera with LED reflection illumination.

The ARF used (Exail IXF-ARF-45-240-V1, Photonics Bretagne) is designed for light guidance at 1550 nm. A scanning electron microscope (SEM) image of the ARF with a microchannel is shown in Fig. 1. To fabricate each microchannel, the fiber was first rotated such that a gap between two of the capillaries was present in the uppermost position. This was achieved by correlating the live image from the top of the fiber with a known reference image as detailed in [27]. This reference image was taken using a short sample of the same fiber which was locked at the desired rotation with a capillary gap at the top, found using the visible end cross-section. The reference image was then taken of the reflected light intensity off the top of the fiber. The fiber sample for machining was then rotated until the correlation coefficient between the reference image and

Optics EXPRESS

the live image was at a maximum. Once the fiber was in the correct rotational orientation, the microchannel was created by first ablating a notch in the fiber layer by layer. This large notch allowed easy debris removal. A hole was then drilled through into the capillary gap to create the microchannel, with minimal disruption to the guiding region. Further details behind this notch design can be found in [27].

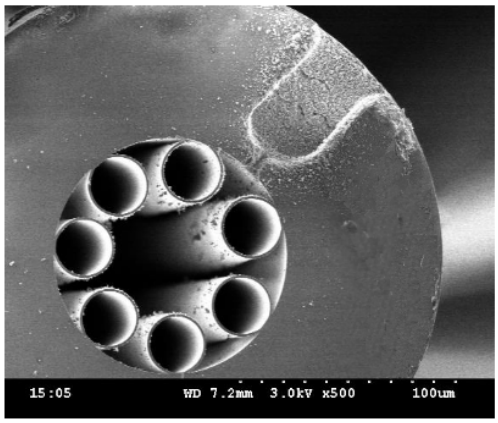

Fig. 1. SEM image of the fabricated microchannel in the anti-resonant hollow-core fiber. Reproduced from [27].

From Fig. 1 it can be seen that the microchannel covers a depth of 50 µm into the fiber. With sufficient debris removal, one 5 × 50 µm microchannel gives 0.056 dB of additional optical loss. A series of microchannels were fabricated at intervals along the fiber perpendicular to the core edge as further detailed in [27]. This is an important quality to ensure the light-guiding capillaries are not damaged from the microchannel fabrication and maximizes the amount of gas which can enter the core. The fiber rotation was adjusted before machining each microchannel to allow for twists in the fiber. This method has the advantage of allowing long lengths of fiber to be machined with close microchannel separation, to achieve high sensitivity and fast response simultaneously.

Two fiber samples were machined, denoted A and B respectively, with different lengths and fabrication parameters to observe the effect of varying microchannel seperation. Cleaved Fiber A was 1 m in length with microchannels located every 5 cm (with 11 cm non-machined length on either end). Cleaved Fiber B was 30 cm in length with microchannels placed every 2 cm (with 2 cm non-machined length at either end). The additional length allowed for the splicing to a single-mode fiber (SMF) bringing the total fiber length post-splicing to around 122 cm and 34 cm.

The diffusion of gas through the core of an ARF, after entering via the microchannels, can be quantified analytically. Hoo *et al.* [29] gives the following equation for the distribution of gas concentration, with a diffusion constant, D, along a holey column of a PCF, which can be considered comparable to the case of ARF [30]:

$$C(x,t) = C_0\left(1 - \frac{4}{\pi}\sum_{j=1,3,5}^{\infty}\frac{1}{j}\left[\sin\left(\frac{j\pi x}{2l}\right)\exp\left(-\frac{j\pi}{2l}\right)Dt\right]\right). \tag{1}$$

Here, C_0 is the concentration of the gas species at the open end of the fiber air column and the diffusion starting point for a gas that has reached position x along the fiber at time t. The path length, and hence consequently the fiber length in this case, is l. From Eq. (1), the average

Optics EXPRESS

concentration of gas species within the fiber of total length L can be calculated by [8]:

$$\bar{C}(t) = \frac{1}{L}\int_0^L C(x,t)\mathrm{d}x = C_0\left(1 - \frac{8}{\pi^2}\sum_{j=1,3,5}^{\infty}\frac{1}{j^2}\exp\left[-\left(\frac{j\pi}{L}\right)^2 Dt\right]\right). \quad (2)$$

3. Experimental setup

The experimental setup is shown in Fig. 2. The fiber sample under test was spliced to SMF using a Sumitomo T-72C fusion splicer. This was performed using the standard settings for SMF-SMF splicing and adapting the parameters to include fiber overlap [31]. By including this setting on the fusion splicer, the two fibers were pushed together in the fiber axis when the electric arc was applied. This ensured that the ARF-SMF splice was fused completely with good mechanical strength. The splicing incurred a transmission loss of 5.25 dB which was acceptable considering there are only two points of splice loss along the path length in Fig. 2. The fiber was placed inside 1/4 inch diameter tubing to ensure the response time of the system was dominated by fiber filling time and not the vessel filling time. The tube ends had vacuum seals around the fiber with a cross piece at one end connected to a vacuum pump, pressure gauge and inlet for the gas sample. The other end of the tube had an outlet for the gas sample. Valves were present on the inlet and outlet.

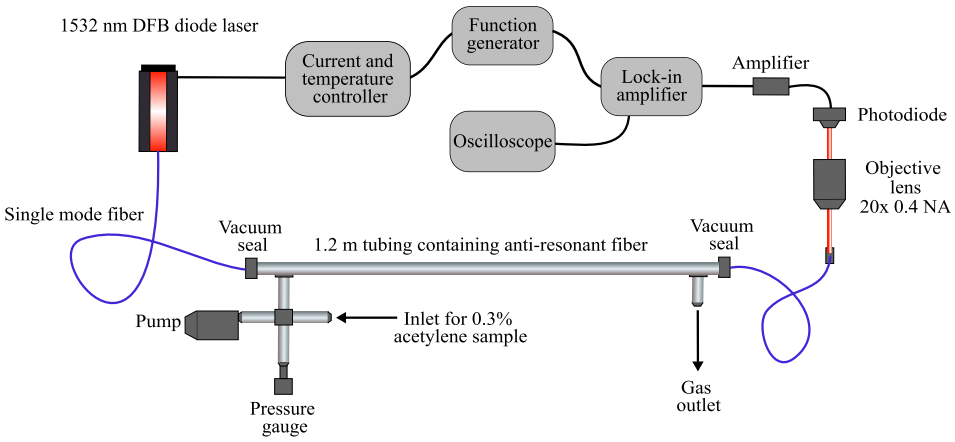

Fig. 2. Diagram of the fiber spectroscopy system. The sample of ARF is contained within 1.2 m of compact vacuum-sealed tubing.

One end of the fiber sample was connected to a 1532 nm DFB laser with FC/APC connectors. The laser was mounted in a Thorlabs laser diode butterfly mount controlled by a combined temperature and current controller (ITC 510), which allowed the laser to be current-tuned. The laser was calibrated with a Burleigh WA-1000 wavemeter and found to have a tuning sensitivity of 0.88 GHz/mA. The other end of the fiber sample was coupled to a photodiode via a 20× 0.4 NA objective mounted on an xyz translation stage. A 20 dB neutral density filter was placed prior to the photodiode to prevent signal saturation. Etalon effects within the optical system were mitigated by purposeful angular misalignment of the components.

The laser current controller was driven by an AIM-TTI 10 MHz DDS function generator. The photodiode output was amplified (femto DLPCA-200) and connected to a LeCroy 200 MHz oscilloscope as well as a Stanford Research Systems DSP lock-in amplifier. The lock-in amplifier reference signal was also connected to the modulation input of the function generator.

Direct absorption spectroscopy was first used to measure the absorption spectrum by tuning the laser frequency and measuring the detected optical power. The strong near-IR absorption lines of

Optics EXPRESS

acetylene were detected by driving the laser with a scanning speed of 25 Hz and a scanning range of 42.4 mA. The amplification for these direct absorption measurements was set to 10^5 V/A with a bandwidth of 400 kHz for Fiber A, and 10^8 V/A with a 7 kHz bandwidth for Fiber B.

Wavelength modulation spectroscopy was also used for enhanced sensitivity. A fast modulation (23.78 kHz sinusoidal) from the lock-in amplifier is imposed on the slowly varying ramp function [32], and the resulting signal on the photodetector is demodulated by the lock-in amplifier at different harmonics of the fast modulation frequency [33]. This technique is advantageous as the detection is shifted to higher frequencies where noise is lower. For the WMS measurements the gain was set to 10^5 V/A with a bandwidth of 400 kHz for Fiber A and 10^7 V/A with a 50 kHz bandwidth for Fiber B.

The chosen test gas was acetylene, which provides easily detectable absorption lines in the near IR, with potential applications in medical diagnostic tests [34]. The initial gas sample was a 0.3% acetylene / 0.3% methane gas mixture balanced in air, first seen tested on Fiber B in earlier work in [24]. The exact quoted concentration of acetylene on the supplied data sheet was 0.276%.

4. Results

4.1. Direct absorption spectroscopy

The acetylene absorption spectrum in the region of interest consists of rotationally-resolved lines belonging to a combination band comprising one quantum of excitation in each of the acetylene C-H stretches and some of these are simulated in Fig. 3 at 293 K, assuming a Voigt profile spectral lineshape. These two absorption lines were measured 60 s after the acetylene valve was opened, to confirm the presence of acetylene in the fiber; the gas having entered via the microchannels. Specifically, the lines are ro-vibrational transitions in the $\nu_1 + \nu_3$ combination band present at wavenumbers, 6526.54 cm^{-1} (P(12e)) and 6529.17 cm^{-1} (P(11e)) and are also shown in Fig. 3. These are P branch transitions with $\Delta J = -1$, where J is the rotational quantum number which charaterises the initial energy state of the molecule. The initial ro-vibrational states are the $J = 12$ and $J = 11$ states, respectively, both with even parity.

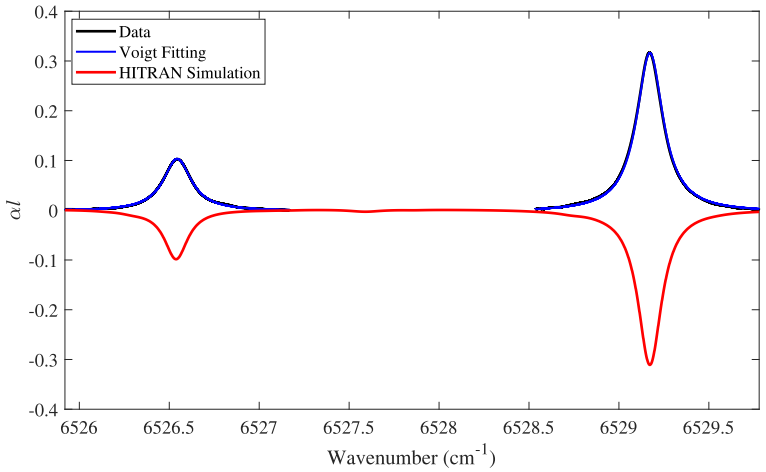

Fig. 3. Direct absorption detected for a 0.276% acetylene gas sample for Fiber A at 6526.54 cm^{-1} and 6529.17 cm^{-1}, fitted with a Voigt profile with the calculated Gaussian width. The simulated HITRAN spectrum is also plotted for comparison. See Data File 1 for the underlying data.

Optics EXPRESS

The target absorption lines occur at the correct wavenumber and relative intensity, and are fitted with a Voigt profile for which the Gaussian component is fixed at that calculated for a temperature of 293 K. Figure 3 gives an example of the Voigt profile fittings for the two lines, taken at atmospheric pressure, compared to a HITRAN simulation of the absorption spectrum for Fiber A. The values of the Lorentzian width and therefore full-width-half-maximum (FWHM) were determined. High-frequency noise was found to be present in the signal of Fiber A, thought to be due to etalon effects from the ARF-SMF splices in the longer fiber, but this was filtered out. The unfiltered signals are also provided in Data File 1. This direct absorption measurement provides a calibration for the harmonics produced from WMS, since the value of α is determined for a known concentration.

4.1.1. Effective path length

The effective path length of light within the fiber, l_{eff}, can be deduced by using the measured value of absorbance, αl, and the Beer-Lambert law. Taking the P(11e) line at 6529.17 cm^{-1}, the integrated cross-section, σ_I, is reported to be 1.165×10^{-20} $cm^2 cm^{-1}$ [35]. Using the ideal gas law to deduce the number density, the effective path lengths for Fiber A and B were found to be equal to 120.17 cm and 31.61 cm, respectively. These values are consistent with the machined fiber lengths (taking into account the excess fiber at either end available for splicing), so it is evident that the entire fiber was filled with the acetylene gas sample.

4.1.2. Pressure broadening parameter

To investigate the effect of pressure in the micro-machined fibers, and to calculate the broadening parameter, γ, the direct absorption lines were also recorded for a variety of pressures using Fiber A. This is to confirm that the fiber responds as expected to changes in pressure, and no unwanted effects arise such as etalon formation. A Voigt fit with a fixed Gaussian width was used to determine the increase in the Lorentzian linewidth. Example Voigt profiles for the P(11e) line are shown in Fig. 4(a). A plot of the half-width-half-maximum (HWHM) against pressure in Fig. 4(b), gives γ equal to 0.080 ± 0.003 cm^{-1}/atm for the P(12e) line and 0.081 ± 0.003 cm^{-1}/atm for the P(11e) line. These are consistent with the HITRAN values of 0.0787 cm^{-1}/atm and 0.0796 cm^{-1}/atm respectively [35]. It should be noted that these values are reported for pure air, whereas the sample used in this section also contains methane, and hence this may be a source of the discrepancy. The Gaussian width is given by the y-axis intercept at zero pressure and is found for the two lines to be 0.014 ± 0.003 cm^{-1} and 0.015 ± 0.004 cm^{-1} respectively, compared to the calculated values in Table 2.

Table 2. Broadening components of the two detected acetylene transitions in Fiber A.

Transition	Wavenumber / cm^{-1}	Calculated Gaussian width at 1 atm and 293 K, w_G / cm^{-1} (GHz)	Lorentzian width, w_L / cm^{-1} (GHz)	FWHM / cm^{-1} (GHz)	Peak value of αl
P(12e)	6526.54	0.015676 (0.46995)	0.1741 (8) (5.22)	0.1754 (3) (5.26)	0.103
P(11e)	6529.17	0.015682 (0.47008)	0.1799 (13) (5.39)	0.1818 (5) (5.45)	0.322

4.2. Wavelength modulation spectroscopy

To further increase the sensitivity of the system, the WMS technique was then implemented. For different gas pressures and therefore line-widths, there exists an optimal modulation amplitude of the laser frequency which will yield the maximum first harmonic amplitude. This can be determined by varying the modulation amplitude, A_{mod}, and recording the subsequent first harmonic amplitude. For the case of Fiber A, at atmospheric pressure, the optimal modulation amplitude was found to be equal to 7.302 GHz using the P(11e) line.

Optics EXPRESS

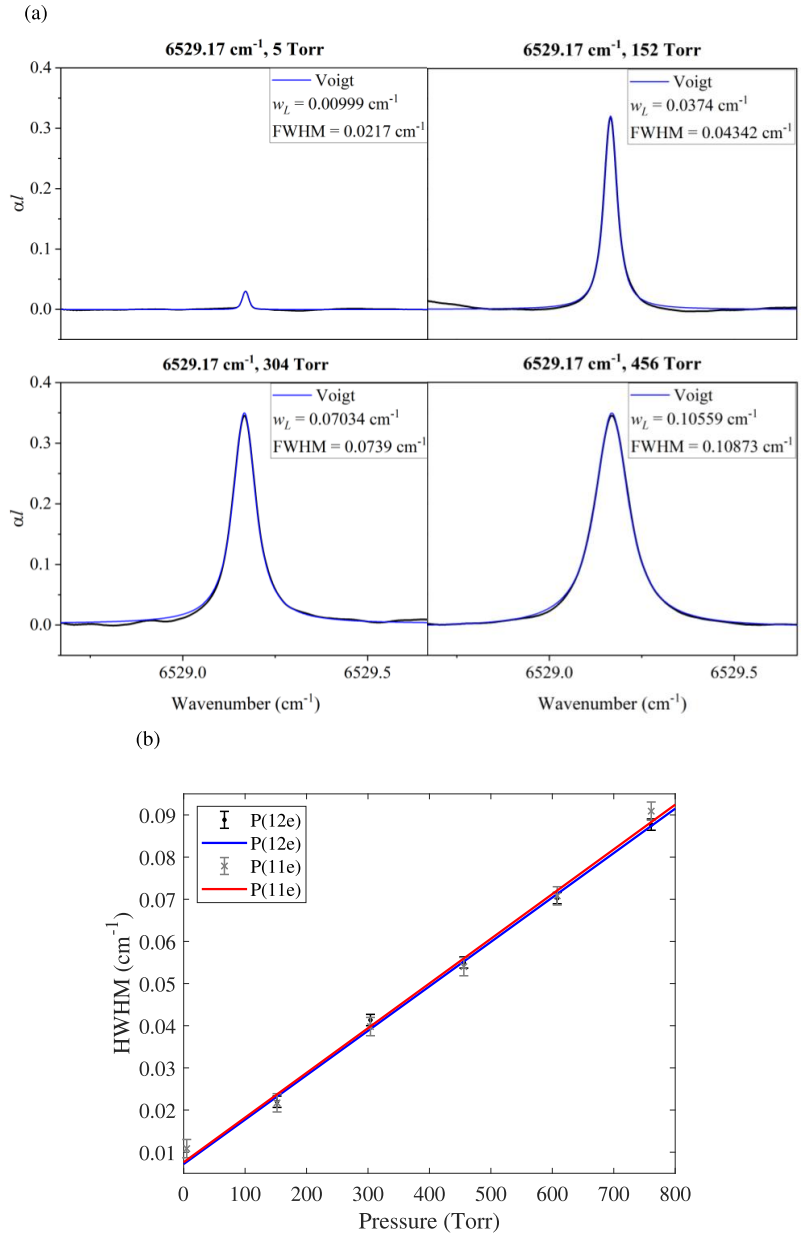

Fig. 4. Calculating the broadening parameter, γ: (a) Examples of the direct absorption lines measured with Fiber A fitted with a Voigt profile at 6529.17 cm^{-1} for a selection of pressures. See Data File 2 for the underlying data. (b) The best fit HWHM as a function of pressure for the P(12e) and P(11e) lines. The error bars on each point were calculated using the standard deviation from the fitted straight line. See Data File 3 for the underlying data. The linewidth errors from the individual line fits in (a) were generally around 1/4 of this value.

Optics EXPRESS

The first harmonics of absorption lines P(12e) and P(11e) were recorded at this optimum modulation depth and where the lock-in sensitivity was set to 50 mV with a 30 µs detection time constant. Figure 5(a) shows this data alongside best fits using theoretical first harmonic lineshapes for Fiber A. The DC baseline offset was measured prior to measurements and accounted for in analysis of the first harmonic signals shown in Fig. 5(a). The calculated Lorentzian widths were 6.95 GHz and 6.79 GHz for the P(12e) and P(11e) lines, respectively. The modulation index, as defined by the ratio of the optimal modulation amplitude to the half width at half maximum, is therefore ~ 2.15 for the P(11e) line. This is consistent with that detailed in [36] as estimated by the value of w_L in this case of a first harmonic. The 0.276% acetylene mixture was then diluted to 0.0276% using nitrogen, to give the first harmonic of the P(11e) transition in Fig. 5(a) using Fiber A at atmospheric pressure. By comparing to the amplitude of the corresponding first harmonic in Fig. 5, this result provides an indication of the low concentrations that the experiment is capable of detecting. The corresponding second harmonics measured at their optimal modulation depth are shown in Fig. 5(b), again for the P(12e) and P(11e) transitions detected using Fiber A. The fast modulation frequency remained the same for this measurement.

4.3. Sensitivity

An overlapping Allan deviation test (OADEV) was carried out on raw 1-f WMS data to show the long-term stability of the system using the P(11e) line, which is shown in Fig. 6. To produce this figure, the signal amplitude was taken at regular intervals over the measurement time of 5 minutes. The Allan deviation refers to the square-root of the Allan variance, which is a metric used to determine the temporal stability of a measurement and hence optimal acquisition time before further averaging leads to no improvement or is even counterproductive [37,38]. The OADEV is an improvement on the original form of the Allan deviation (or variance) based on a development by Snyder [39] where many overlapping series are generated from the measurement dataset. The method is equivalent to averaging the measurement samples in blocks prior to the processing for the analysis and has been found to give a more accurate Allan variance [40].

It is clear that after an integration time of ~ 100 s, the Allan deviation, σ_A (V), is minimised and the measurement has highest sensitivity. It must be noted however that shorter integration times may be sufficient depending upon the specific application, and the short time response presented in the next section may be a more applicable measure of the time needed to produce a useful and detectable absorption signal.

The sensitivity and minimum detection limit can therefore be determined by quantifying the maximum detected first harmonic amplitude and the standard deviation of the baseline at 100 s integration time. For Fiber A, the measured value of αl from the direct absorption, the signal-to-noise ratio and the effective path length were used to quantify a minimum detectable αl value, which was found to be 4.43×10^{-5}. For the 120.17 cm path length, $\alpha_{min} = 3.69 \times 10^{-7}$ cm^{-1}. This is equivalent to 380 parts per billion at atmospheric pressure. This will be compared to Fiber B later in this work.

4.4. Response time

The time response of each fiber was measured by recording the first harmonic amplitude over time at a gas flow rate of 0.2 SLM. The flow rate was also varied between 0.025 SLM and 0.8 SLM with no change in the time response or fiber filling time observed, indicating that under these conditions the limiting factor is the microchannel separation. These data can be found in Data File 7. The amplitude of the first harmonic signal was converted into a concentration using the calibration from the direct absorption spectroscopy in Section 4.1, which gives the amount of absorbance for the known gas concentration. Figure 7(a) shows the measured concentration against time for Fibers A and B. For comparison, Fig. 7(b) shows the theoretical $\bar{C}/C_0$ for fibers

Optics EXPRESS

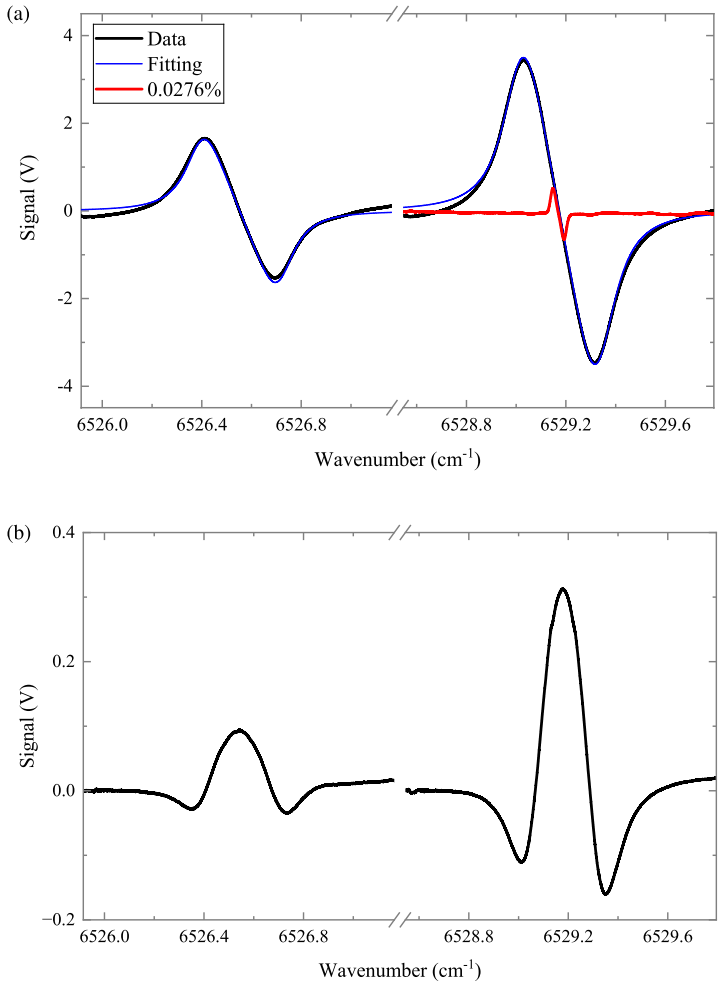

Fig. 5. Harmonics detected for Fiber A for a 0.276% acetylene gas sample at line centers 6526.54 cm^{-1} and 6529.17 cm^{-1}: (a) First harmonics at the optimal modulation amplitude, 7.302 GHz. Also shown is the first harmonic of the 0.0276% acetylene gas for the 6529.17 cm^{-1} line. See Data File 4 for the underlying data. (b) Second harmonics. See Data File 5 for the underlying data.

with the corresponding microchannel separations of 5 cm and 2 cm. These results show good agreement between the experimental results and the theoretical predictions.

To model the diffusion of the gas along the fiber after entering the microchannels, Eq. (2) gives the average concentration at time, t, integrated over the fiber length, L. The difference in this case is that there are two sources of concentration, one from each microchannel either side of the section of fiber under consideration. As both fluxes are towards the center of the fiber length between microchannels, the difference will be the total flux, $J = J_1 + J_2$. Since the flow and concentration of gas are the same for each microchannel, this introduces a factor of 2 into the diffusion flux, and this propagates through as a factor of $2D$. For an acetylene gas sample, the diffusion coefficient in air is quoted to be 0.146 cm^2/s [41]. Using Eq. (2), the time response of $\bar{C}/C_0$ can be determined for different microchannel separations.

Optics EXPRESS

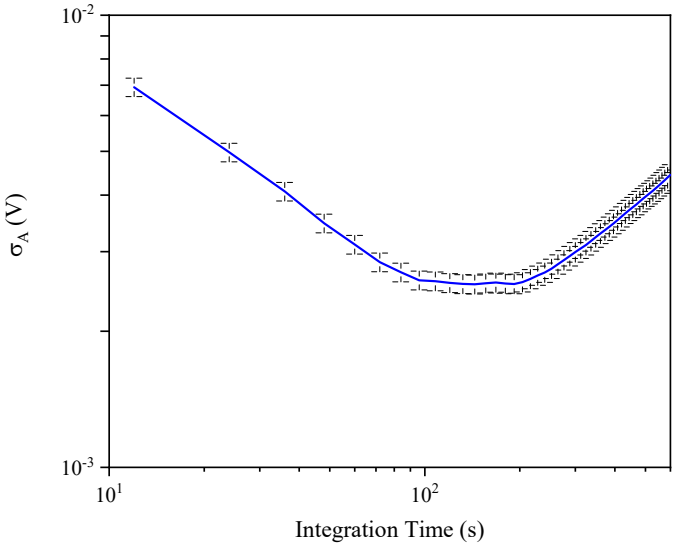

Fig. 6. Allan deviation analysis on raw 1-f WMS data showing the long-term stability of the absorption measurement. The deviation no longer continues to improve after ~ 100 s. (See Data File 6 for the underlying data). The Allan deviation can be readily converted to absorption or concentration using a predetermined calibration from the direct absorption.

The fiber filling time and hence response time of the fiber can be evaluated by the amount of time it takes for the absorption to increase from 10% to 90% of the maximum amplitude [17]. It should be noted, however, that it is not essential for the entire fiber to fill and the harmonic amplitude to be maximal for a clear absorption to be seen, as shown by the rapid increase in signal amplitude after 5 s as shown in Fig. 7(a). The timescale for this is on the order of 100 ms. The magnitude of the first harmonic reaches the 90% value after 22 s for Fiber A and 4.2 s for Fiber B. This is compared to a value calculated by Eq. (2) for the case of no microchannels where this same quantity is 3 hours and 14.7 minutes respectively. It appears that there is an initial fast response and a longer exponential increase of the first harmonic amplitude. With comparison to results shown in the literature in Table 1, for the length scales of 1 m of fiber, this is a promising result for a near-IR fiber gas sensor. There is simultaneously a high sensitivity (380 ppb) and a fast response time (22 s), quantified by the fiber filling time, without the use of a pressure differential.

4.5. Comparison

To compare the two fiber samples, the minimum detection limit of Fiber B was also quantified using the same techniques as Section 4.3. An Allan deviation found a 240 s integration time for this fiber. However, in this case, the early results in [24] were improved in this work by using a higher concentration 5% acetylene in nitrogen mixture to give a clear direct absorption and first harmonic with an improved signal-to-noise ratio. When the 4.96% C_2H_2 sample was used in Fiber B, the maximum/peak value of αl for the P(11e) line was found to be 1.51 as expected for a 3× shorter fiber but a 16× higher concentration compared to the value of 0.322 for the same transition for Fiber A in Table 2. The absorption results found therefore remain consistent with the change in parameters between Fibers A and B. In an additional test of Fiber A at the higher 4.96% concentration, it was also found that the time to reach the maximum first harmonic

Optics EXPRESS

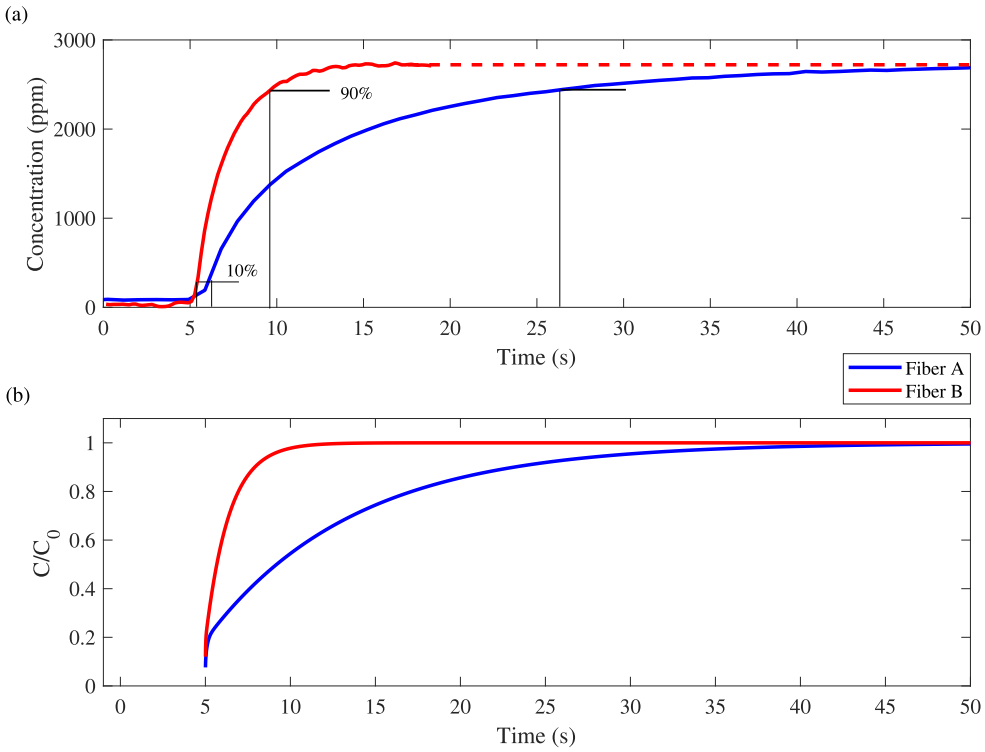

Fig. 7. (a) The recorded increase in the concentration of acetylene at 0.2 SLM flow rate for Fiber A (5 cm microchannel separation) and Fiber B (2 cm microchannel separation). The gas sample was introduced to the fiber tubing at 5 s, and the 10% to 90% time response can be seen. See Data File 8 for the underlying data. (b) Theoretical prediction of concentration for microchannel separations of 2 cm and 5 cm for comparison. A comparison with the development predicted by Eq. (2) shows good agreement.

amplitude was consistent with the experiment conducted with the lower 0.276% concentration gas sample.

The potential for an improved time response of 4.2 s is shown by using closer microchannel separation in Fiber B. With improvements and optimization of the microchannel fabrication system [27], even longer lengths of fiber could be machined with closer hole separation to push both of these quantities further. A comparison of the optimal results of the two tested fibers is shown in Table 3. Due to the nature of the microchannels, the fiber filling time will only be affected by microchannel separation rather than fiber length [42]; this is consistent with the decrease in filling time between the 5 cm and 2 cm separation.

Table 3. Comparison of the optimal results obtained using Fiber A and Fiber B of the machined ARF.

Fiber	A	B
Microchannel Separation (cm)	5	2
Minimum Detection Limit (α_{min} (cm^{-1}))	3.69×10^{-7} / 380 ppb (at 0.276% C_2H_2)	1.56×10^{-5} / 16.8 ppm (at 4.96% C_2H_2)
Fiber Filling Time (10% to 90%) (s) at 0.2 SLM	22	4.2

Optics EXPRESS

5. Conclusion

This work has demonstrated a hollow-core optical fiber based gas sensor with simultaneous high sensitivity and fast response time. This was achieved using 1 m of anti-resonant hollow-core fiber with a series of microchannels fabricated in the side every 5 cm. Femtosecond laser ablation was used to fabricate through the capillary gap into the hollow fiber core. The optimum fiber orientation was obtained using imaging from the side, thereby allowing closely-spaced microchannels along long lengths of fiber. Measurements using wavelength modulation spectroscopy on a 0.3% acetylene gas mixture balanced in nitrogen showed an acetylene detection limit of 380 parts per billion at 100 s integration time, and a fast fiber filling time of 22 s, a competitive and promising result when compared to current literature values in Table 1. The filling time, and therefore overall time response, also agrees well with that expected from analytical equations describing diffusion in hollow fibers. The potential for a faster time response was shown using a separate 30 cm fiber sample with a microchannel separation of 2 cm, with a shorter fiber filling time of 4.2 s. With improvements and optimization of the microchannel fabrication procedure, these quantities can be improved further. This includes better debris removal practices to reduce light loss and increased machining automation to allow for longer fiber to be produced with closer spaced microchannels. Additionally, future applications may require the fiber to be bent. Improved physical robustness of the fiber could be achieved by machining through the fiber coating or reducing the dimensions of the notch in [27]. Further improvements to the detection system, such as utilising a quartz tuning fork could enhance the sensor performance and reduce equipment size and costs [43].

Funding. Engineering and Physical Sciences Research Council (EP/T00326X/1, EP/W025256/1, EP/T517811/1, 2595670).

Disclosures. The authors declare no conflicts of interest.

Data availability. Data supporting the results in this paper are provided in the supplementary information.

References

1. J. B. McManus, M. S. Zahniser, D. D. Nelson, *et al.*, "Recent progress in laser-based trace gas instruments: performance and noise analysis," Appl. Phys. B **119**(1), 203–218 (2015).
2. R. N. Zare, D. S. Kuramoto, C. Haase, *et al.*, "High-precision optical measurements of $^{13}C/^{12}C$ isotope ratios in organic compounds at natural abundance," Proc. Natl. Acad. Sci. **106**(27), 10928–10932 (2009).
3. F. Yu and J. C. Knight, "Negative curvature hollow-core optical fiber," IEEE J. Sel. Top. Quantum Electron. **22**(2), 146–155 (2016).
4. M. Nikodem, K. Krzempek, G. Dudzik, *et al.*, "Hollow core fiber-assisted absorption spectroscopy of methane at 3.4 µm," Opt. Express **26**(17), 21843–21848 (2018).
5. F. Yang, W. Jin, Y. Cao, *et al.*, "Towards high sensitivity gas detection with hollow-core photonic bandgap fibers," Opt. Lett. **22**(20), 24894–24907 (2014).
6. Y. L. Hoo, L. Shujing, L. H. Ho, *et al.*, "Fast response microstructured optical fiber methane sensor with multiple side-openings," IEEE Photonics Technol. Lett. **22**(5), 296–298 (2010).
7. J. P. Carvalho, H. Lehmann, H. Bartelt, *et al.*, "Remote system for detection of low-levels of methane based on photonic crystal fibres and wavelength modulation spectroscopy," J. Sens. **2009**(1), 1 (2009).
8. J. P. Parry, B. C. Griffiths, N. Gayraud, *et al.*, "Towards practical gas sensing with micro-structured fibres," Meas. Sci. Technol. **20**(7), 075301 (2009).
9. P. Jaworski, P. Kozioł, K. Krzempek, *et al.*, "Antiresonant hollow-core fiber-based dual gas sensor for detection of methane and carbon dioxide in the near- and mid-infrared regions," Sensors **20**(14), 3813 (2020).
10. P. Jaworski, K. Krzempek, G. Dudzik, *et al.*, "Nitrous oxide detection at 5.26 µm with a compound glass anti-resonant hollow-core optical fiber," Opt. Lett. **45**(6), 1326–1329 (2020).
11. C. Yao, L. Xiao, S. Gao, *et al.*, "Sub-ppm CO detection in a sub-meter-long hollow-core negative curvature fiber using absorption spectroscopy at 2.3 µm," Sens. Actuators, B. Chem. **303**, 127238 (2020).
12. M. Nikodem, G. Gomólka, M. Klimczak, *et al.*, "Laser absorption spectroscopy at 2 µm inside revolver-type anti-resonant hollow core fiber," Opt. Express **27**(10), 14998–15006 (2019).
13. M. Nikodem, G. Gomólka, M. Klimczak, *et al.*, "Demonstration of mid-infrared gas sensing using an anti-resonant hollow core fiber and a quantum cascade laser," Opt. Express **27**(25), 36350–36357 (2019).
14. H. Arman, S. Olyaee, and M. Seifouri, "Numerical optimization of anti resonant hollow core fiber for high sensitivity methane detection," Sci. Rep. **14**(1), 31534 (2024).

Optics EXPRESS

15. G. Gomólka, G. Stepniewski, D. Pysz, *et al.*, "Highly sensitive methane detection using a mid-infrared interband cascade laser and an anti-resonant hollow-core fiber," Opt. Express **31**(3), 3685–3697 (2023).
16. J. Kapit and A. P. M. Michel, "Dissolved gas sensing using an anti-resonant hollow core optical fiber," Appl. Opt. **60**(33), 10354–10358 (2021).
17. P. Kozioł, P. Bojes, P. Jaworski, *et al.*, "Enhancing gas diffusion in antiresonant hollow-core fiber gas sensors using microchannels," Photonic Sens. **15**(3), 250336 (2025).
18. P. Gronowicz, G. Gomólka, D. Pysz, *et al.*, "Demonstration of a compact reflective gas sensing probe based on a negative-curvature hollow-core fiber," Appl. Opt. **64**(20), 5624–5631 (2025).
19. A. D. Pryamikov, "Negative curvature hollow core fibers: design, fabrication, and applications," in *Proc. SPIE LASE*, (San Francisco, California, United States, 2014).
20. A. D. Pryamikov, A. S. Biriukov, A. F. Kosolapov, *et al.*, "Demonstration of a waveguide regime for a silica hollow - core microstructured optical fiber with a negative curvature of the core boundary in the spectral region > 35 μm," Opt. Express **19**(2), 1441–1448 (2011).
21. E. Numkam Fokoua, S. Abokhamis Mousavi, G. T. Jasion, *et al.*, "Loss in hollow-core optical fibers: mechanisms, scaling rules, and limits," Adv. Opt. Photonics **15**(1), 1–85 (2023).
22. C. Wei, C. R. Menyuk, and J. Hu, "Impact of cladding tubes in chalcogenide negative curvature fibers," IEEE Photonics J. **8**(3), 1–9 (2016).
23. T. Allsop and R. Neal, "A review: Application and implementation of optic fibre sensors for gas detection," Sensors **21**(20), 6755 (2021).
24. E. A. Warrington, R. Peverall, P. S. Salter, *et al.*, "A high sensitivity, fast response optical fiber gas sensor using micro-drilled anti-resonant fiber," *28th International Conference on Optical Fiber Sensors*, Technical Digest Series (Optica Publishing Group, 2023), paper Tu3.10. (2023).
25. P. Kozioł, P. Jaworski, K. Krzempek, *et al.*, "Fabrication of microchannels in a nodeless antiresonant hollow-core fiber using femtosecond laser pulses," Sensors **21**(22), 7591 (2021).
26. K. Krzempek, P. Jaworski, P. Koziol, *et al.*, "Antiresonant hollow core fiber-assisted photothermal spectroscopy of nitric oxide at 5.26 μm with parts-per-billion sensitivity," Sens. Actuators, B. Chem. **345**, 130374 (2021).
27. E. A. Warrington, P. S. Salter, W. O. C. Davis, *et al.*, "Micro-drilling hollow-core fiber using image processing for rotational alignment," Opt. Express **33**(11), 23616–23629 (2025).
28. B. N. Chichkov, C. Momma, S. Nolte, *et al.*, "Femtosecond, picosecond and nanosecond laser ablation of solids," Appl. Phys. A **63**(2), 109–115 (1996).
29. Y. L. Hoo, W. Jin, H. L. Ho, *et al.*, "Gas diffusion measurement using hollow-core photonic bandgap fiber," Sens. Actuators, B. Chem. **105**(2), 183–186 (2005).
30. J. Crank, *The Mathematics of Diffusion*, 2nd Edition (Oxford, 2008), chap. 4, pp. 47–64.
31. Y. Min, A. Filipkowski, G. Stepniewski, *et al.*, "Fusion splicing of silica hollow core anti-resonant fibers with polarization maintaining fibers," J. Lightwave Technol. **39**(10), 3251–3259 (2021).
32. Y. Ma, W. Feng, S. Qiao, *et al.*, "Hollow-core anti-resonant fiber based light-induced thermoelastic spectroscopy for gas sensing," Opt. Express **30**(11), 18836–18844 (2022).
33. S. Schilt, L. Thévenaz, and P. Robert, "Wavelength modulation spectroscopy: Combined frequency and intensity laser modulation," Appl. Opt. **42**(33), 6728–6738 (2003).
34. J. S. Sadeh, A. Miller, and M. L. Kukin, "Noninvasive measurement of cardiac output by an acetylene uptake technique and simultaneous comparison with thermodilution in ICU patients," Chest **111**(5), 1295–1300 (1997).
35. I. E. Gordon, L. S. Rothman, R. J. Hargreaves, *et al.*, "The HITRAN2020 molecular spectroscopic database," J. Quant. Spectrosc. **277**, 107949 (2022).
36. T. R. S. Hayden and G. B. Rieker, "Large amplitude wavelength modulation spectroscopy for sensitive measurements of broad absorbers," Opt. Express **24**(24), 27910–27921 (2016).
37. R. Schieder, E. L. Kollbery, G. Rau, *et al.*, "Characterization and measurement of system stability," in *Proc. 1985 International Technical Symposium/Europe*, (Cannes, France, 1986).
38. D.-B.-A.-. Tran, R. Peverall, S. Rosson, *et al.*, "High performance continuous-wave laser cavity enhanced polarimetry using rf-induced linewidth broadening," Opt. Express **29**(19), 30114–30122 (2021).
39. J. J. Snyder, "An ultra-high resolution frequency meter," in *Proc. Thirty Fifth Annual Frequency Control Symposium*, (1981).
40. D. A. Howe, D. U. Allan, and J. A. Barnes, "Properties of signal sources and measurement methods," in *Proc. Thirty Fifth Annual Frequency Control Symposium*, (1981).
41. M. J. Tang, M. Shiraiwa, U. Pöschl, *et al.*, "Compilation and evaluation of gas phase diffusion coefficients of reactive trace gases in the atmosphere: Volume 2. diffusivities of organic compounds, pressure-normalised mean free paths, and average knudsen numbers for gas uptake calculations," Atmos. Chem. Phys. **15**(10), 5585–5598 (2015).
42. J. Karp, W. Challener, M. Kasten, *et al.*, "Fugitive methane leak detection using mid-infrared hollow-core photonic crystal fiber containing ultrafast laser drilled side-holes," in *Proc. SPIE Commercial + Scientific Sensing and Imaging*, Vol. 9852, (Baltimore, Maryland, United States, 2016).
43. S. Qiao, Z. Lang, Y. He, *et al.*, "Calibration-free measurement of absolute gas concentration and temperature via light-induced thermoelastic spectroscopy," Adv. Photonics **7**(06), 066007 (2025).